J. Fluid Mech. (1994), *vol.* 279, *pp.* 135–163

Motion of a deformable capsule through a hyperbolic constriction

By ANNE LEYRAT-MAURIN
AND DOMINIQUE BARTHES-BIESEL
Université de Technologie de Compiègne, URA CNRS 858, BP 649,
60 206 Compiègne Cedex, France

(Received 5 July 1993 and in revised form 1 June 1994)

A model for the low-Reynolds-number flow of a capsule through a constriction is developed for either constant-flow-rate or constant-pressure-drop conditions. Such a model is necessary to infer quantitative information on the intrinsic properties of capsules from filtration experiments conducted on a dilute suspension of such particles. A spherical capsule, surrounded by an infinitely thin Mooney–Rivlin membrane, is suspended on the axis of a hyperbolic constriction. This configuration is fully axisymmetric and allows the entry and exit phenomena through the pore to be modelled. An integral formulation of the Stokes equations describing the flow in the internal and external domains is developed. It provides a representation of the velocity at any location in the flow as a function of the unknown forces exerted by the boundaries on the fluids. The problem is solved by a collocation technique in the case where the internal and external viscosities are equal. Microscopic quantities (instantaneous geometry, centre of mass velocity, elastic tensions in the membrane) as well as macroscopic quantities (entry time, additional pressure drop or flow rate reduction) are predicted as a function of the capsule intrinsic properties and flow characteristics. The results obtained for a capsule whose initial diameter is larger than that of the constriction throat show that the maximum energy expenditure occurs when the particle centre of mass is still upstream of the throat (typically 1 diameter away), and is thus due to the entry process. For large enough or rigid enough capsules, the model predicts entrance or exit plugging, in agreement with experimental observations. It is then possible to correlate the variation of the pore hydraulic resistance to the flow capillary number (ratio of viscous to elastic forces) and to the size ratio between the pore and the capsule.

1. Introduction

Encapsulation is an active field of research with applications in medicine, pharmaceutics and industry. The development of relevant techniques to assess the mechanical properties of encapsulated drops originates with the study of blood cells. A number of experimental techniques such as viscometry and filtration have been designed, spurring the development of mechanical and rheological models for the quantitative interpretation of the results. The behaviour of a capsule in flow is difficult to study because of the strongly coupled nature of the fluid/structure interactions that govern its motion and deformation. A further complication is due to the large number of parameters involved, such as the initial geometry of the particle or the internal liquid and membrane rheological properties.

A few models are available for the interpretation of experimental data obtained with

devices measuring capsule deformability. The common principle underlying most of them is to predict the motion and deformation of a single capsule as a function of the internal viscosity and membrane mechanical properties. Analytical three-dimensional models are available for initially spherical capsules under moderate deformations (Barthes-Biesel & Rallison 1981; Barthes-Biesel & Sgaier 1985) or for ellipsoidal capsules with an assigned deformed geometry (Keller & Skalak 1982; Tran-Son-Tay, Sutera & Rao 1984). These models can be used to analyse direct observations of capsules in a shear flow (Sutera, Pierre & Zahalak 1989; Chang & Olbricht 1993), and also allow the derivation of rheological constitutive equations for dilute suspensions of identical capsules by averaging the contribution from all the particles (Drochon *et al.* 1990). The dilution assumption is necessary to guarantee the absence of interaction between the particles. These equations then allow the interpretation of rheological data in terms of the particles' mechanical properties. The spherical capsule analyses have so far been confined to moderate deformations and, therefore, they have a limited range of validity.

The study of large deformations of capsules was made possible by the development of boundary integral formulations of Stokes flow (Ladyzhenskaya 1969). Youngren & Acrivos (1975) developed and numerically implemented this method to study the slow viscous flow of an unbounded fluid past an arbitrary solid particle. The cases of a gas bubble (Youngren & Acrivos 1976) and of a liquid droplet (Rallison & Acrivos 1978) in elongational flow were studied shortly thereafter. The method was extended by Li, Barthes-Biesel & Helmy (1988) to the study of large deformations of initially ellipsoidal capsules with a Mooney–Rivlin membrane, suspended in an elongational flow. Using the same flow configuration, Pozrikidis (1990) considered capsules with a red-blood-cell-type membrane with an incompressible interface. The main contribution of these studies is to show clearly the effect of different interfacial constitutive behaviour on the overall capsule distortion. However, the study of capsules under large deformation has so far been confined to pure elongational flows which are of limited applicability to real problems.

The modelling of filtration flows has not been addressed yet, although situations where capsules are moving through ducts have already been tackled. Helmy & Barthes-Biesel (1982) used a perturbation method to study the migration of a small initially spherical capsule with a Mooney–Rivlin membrane in a Poiseuille flow. In the case of closely fitting particles, the existence of a thin film of liquid between the particle and the capillary wall allows one to use the lubrication theory to evaluate the pressure gradient in the film. Rigid particles, deformable particles, and capsules have been studied with this method (Tözeren & Skalak 1979; Secomb *et al.* 1986). Unfortunately, some of these models require specific shapes, and most of them address steady configurations. As a consequence, they are not useful to analyse filtration experiments that are essentially transient nor situations in which entrance/exit effects in the pore are clearly important.

It is the objective of this paper to provide a model for a quantitative analysis of filtration experiments conducted with dilute suspensions of capsules, i.e. to describe the motion and deformation of a single capsule flowing through a hyperbolic pore. The formulation of the present problem complements that of Li *et al.* (1988) and is similar to that used by Martinez & Udell (1990) for neutrally buoyant drops flowing through circular tubes at constant flow rate. The difference here, as compared to the elongational case of Li *et al.*, comes from the presence of solid boundaries, the influence of which must be included. Furthermore, either constant-pressure-drop or constant-flow-rate conditions are modelled. Owing to the space-varying channel

geometry, flow is transient and dominated by entrance and exit effects. The hyperbolic constriction represents a short pore or a thin filtration membrane, and has the advantage that the undisturbed flow field is known analytically.

The formulation of the Stokes equations in both the internal and suspending liquid of the capsule using the boundary integral method is well adapted to this type of strongly nonlinear free boundary problem, where the shape of one of the boundaries is unknown *a priori* and must therefore be determined as part of the solution. The advantage of this technique is to avoid solving the Stokes equations in their differential form throughout the whole flow domain by relating the velocity of any point within the fluid to the velocity and stresses on the boundaries.

The present study focuses on initially spherical capsules, which have a radius at least 20 % larger than the throat radius, in their resting shape. Furthermore, the internal and external liquids have the same viscosity. This last condition results in a significant simplification of the model. From the experimental point of view, Drochon *et al.* (1993) have shown that red-blood-cell membrane rigidification could be detected by means of filtration experiments, provided one used a suspending medium with a viscosity roughly equal to that of the internal haemoglobin solution.

A Mooney–Rivlin constitutive law is selected for the membrane. This choice corresponds to the simplest elastic behaviour, and is appropriate for elastomer membranes or for interfaces obtained by interfacial cross-linking polymerization. The model provides the velocity of points on the capsule membrane and therefore predicts the evolution of the capsule shape as it flows through the constriction. At each time step, local variables are computed at the microscopic level, such as capsule geometry, centre of mass velocity, and elastic tensions in the membrane. Global quantities at the macroscopic level of the overall flow, are also predicted at each time step. These include the entry time of the capsule through the pore, the additional pressure drop or the perturbation of flow rate (according to the type of flow condition chosen, respectively constant flow rate or constant pressure head) or correspondingly, the hydraulic resistance of the system. Among the model parameters are the capillary number, which measures the ratio between viscous and elastic forces to which the membrane is subjected, the initial shape of the capsule and the size ratio between its characteristic dimension and the radius of the constriction throat.

Constant-pressure-drop flows are considered in the first part of the discussion. A detailed study of the micromechanics of a capsule at positions corresponding to particular values of the macroscopic quantities characterizing the flow is presented. First, capsules that are deformable enough to pass through the throat without touching the walls or exhibiting membrane failure are considered. In this generic class, the influence of the capillary number and size ratio is studied. A description of the theoretical occurrence of pore plugging as a function of the capillary number and size ratio, along with a discussion of the limits of validity of the model are then presented. The dependence of the maximum flow rate perturbation and of the entry time of the capsule into the pore on the capsule size and properties is discussed. The influence of switching to a constant-flow-rate condition is then investigated. The effect of the type of flow on the passage of the capsules and on the occurrence and types of plugging at different values of the capillary number and size ratio is outlined.

2. Problem statement

The formulation of the problem applies to general three-dimensional situations, but for simplicity, a fully axisymmetric configuration is considered (figure 1), in which the

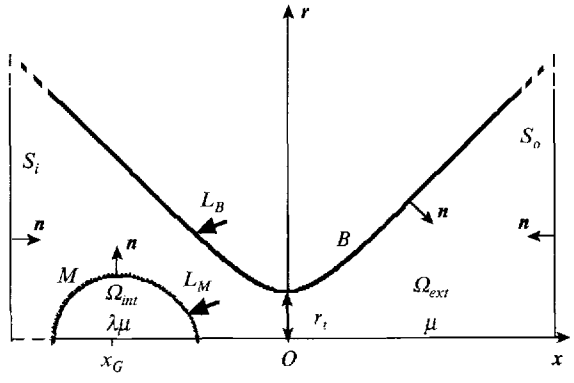

FIGURE 1. Schematic of the problem.

channel is a hyperboloid with revolution axis Ox. The velocity $\boldsymbol{v}^{np}(\boldsymbol{x})$ and pressure $P^{np}(\boldsymbol{x})$ fields have been determined exactly by Happel & Brenner (1965), for the Stokes flow of a Newtonian incompressible liquid with viscosity μ. In particular, it is found that far from the throat, the pressure is uniform, and the total pressure drop ΔP^{np} across the constriction is related to the volume flow rate Q by

$$\Delta P^{np} = \frac{\mu Q}{r_t^3} R_H,$$

where r_t is the throat radius. The pore hydraulic resistance R_H depends only on geometry and is given by

$$R_H = \frac{3(1-\zeta_0^2)^{3/2}}{(1+2\zeta_0)(1-\zeta_0)^2},$$

where ζ_0 is the cosine of the angle of the hyperbola asymptote with the axis. The resistance R_H varies between 3 ($\zeta_0 = 0$, hole in a plane, also called Sampson flow) and infinity ($\zeta_0 = 1$, infinitely long cylindrical duct).

The capsule consists of a drop of a Newtonian incompressible fluid of viscosity $\lambda\mu$ surrounded by an infinitely thin membrane (M) with negligible bending resistance and with a surface shear elastic modulus E_s. In its unstressed state, the capsule is a sphere with radius Rr_t. At the beginning of the computational time, the capsule is injected into the flow, with its centre of mass at the axis.

Non-dimensional quantities are used throughout, based on the following scales: r_t for lengths, E_s for elastic tensions, V_0 (the average throat velocity of the flow at time $t = 0$) for velocities, $\mu V_0/r_t$ for viscous stresses.

To model a wide range of filtration devices, the flow through the constriction is driven either by a constant flow rate or by a constant pressure drop. In the first case, the total pressure drop $\Delta P(t)$ varies with time, and the bulk boundary conditions for the flow are then

$$\Delta P(t) = R_H \pi + \Delta P_{add}(t), \quad Q(t) = \pi, \tag{2.1}$$

where $\Delta P_{add}(t)$ represents the additional pressure drop due to the capsule. In the second case, the flow rate varies with time and the bulk boundary conditions are

$$\Delta P(t) = R_H \pi, \quad Q(t) = \pi - \frac{\Delta P_{add}(t)}{R_H}. \tag{2.2}$$

In the latter case, the unperturbed far-field velocity $\boldsymbol{v}^{np}(\boldsymbol{x}, t)$ that occurs in the absence of the capsule, is a function of time.

2.1. *Equations of motion for the fluids*

We introduce a fixed cylindrical frame of reference (x, r, ϕ) (figure 1) centred on the revolution axis at the throat of the constriction. The domains occupied by the internal and external liquids are respectively denoted Ω_{int} and Ω_{ext}. Normal unit vectors $\boldsymbol{n}$ point into Ω_{ext}. The capsule membrane, channel walls, inlet and outlet sections are denoted respectively M, B, S_i and S_o. The fluid domain Ω_{int} is therefore bounded by M, and Ω_{ext} is bounded by M, B, S_i and S_o. Under the assumption that the particle Reynolds number is very small, the velocity $\boldsymbol{v}$ and pressure p in the internal and external fluids are governed by the Stokes equations:

$$\left.\begin{aligned} &\nabla\cdot\boldsymbol{\sigma}^{int} = 0, \quad \nabla\cdot\boldsymbol{v}^{int} = 0 \quad \text{in} \quad \Omega_{int},\\ &\nabla\cdot\boldsymbol{\sigma}^{ext} = 0, \quad \nabla\cdot\boldsymbol{v}^{ext} = 0 \quad \text{in} \quad \Omega_{ext},\\ \text{with}\qquad &\boldsymbol{\sigma}^{int} = -p\boldsymbol{I} + \lambda(\nabla\boldsymbol{v}^{int} + {}^{T}\nabla\boldsymbol{v}^{int}) \quad \text{in} \quad \Omega_{int},\\ &\boldsymbol{\sigma}^{ext} = -p\boldsymbol{I} + (\nabla\boldsymbol{v}^{ext} + {}^{T}\nabla\boldsymbol{v}^{ext}) \quad \text{in} \quad \Omega_{ext}, \end{aligned}\right\} \tag{2.3}$$

where $\boldsymbol{\sigma}^{ext}$ and $\boldsymbol{\sigma}^{int}$ are the stress tensors and $\boldsymbol{v}^{ext}$ and $\boldsymbol{v}^{int}$ the velocity fields in the external and internal domains, respectively.

For convenience, the sections S_i and S_o are assumed to be symmetrical with respect to the throat, located at a distance L from the throat that is large enough for the undisturbed pressures to be uniform to $O(L^{-3})$ and the radial and axial velocities to be vanishingly small, i.e. $O(L^{-3})$ and $O(L^{-2})$ respectively. Furthermore, S_i and S_o are required to be far enough from the capsule for the velocity perturbation to be negligible:

$$\boldsymbol{v}^{ext}(\boldsymbol{x}, t) \to \boldsymbol{v}^{np}(\boldsymbol{x}, t) \approx 0, \quad \boldsymbol{x} \in S_i \quad \text{or} \quad S_o. \tag{2.4}$$

These conditions guarantee that the flow through S_i or S_o is characterized by vanishing velocities even when the capsule is present. The pressure in these sections (P_i and P_o respectively) is uniform but unknown. Their difference is $\Delta P(t)$, the instantaneous pressure drop across the constriction (equations (2.1) or (2.2)).

The no-slip boundary condition is required on the solid wall of the constriction B and on the deformed surface of the membrane:

$$\boldsymbol{v}^{ext}(\boldsymbol{x}, t) = 0, \quad \boldsymbol{x} \in B, \tag{2.5}$$

$$\boldsymbol{v}^{ext}(\boldsymbol{x}, t) = \boldsymbol{v}^{int}(\boldsymbol{x}, t) = \partial\boldsymbol{x}/\partial t \quad \text{for} \quad \boldsymbol{x} \in M. \tag{2.6}$$

Finally, the dynamic equilibrium of the membrane leads to

$$\epsilon(\boldsymbol{\sigma}^{ext} - \boldsymbol{\sigma}^{int})\cdot\boldsymbol{n} + \boldsymbol{p} = 0 \quad \text{for} \quad \boldsymbol{x} \in M, \tag{2.7}$$

where $\boldsymbol{p}$ is the force per unit area of deformed surface exerted by the membrane on the surrounding liquids. Once the velocity of the membrane points is known, the integration of the kinematic condition (2.6) yields the displacement of the membrane points and therefore allows the computation of the shape of the membrane at any time. Then, $\boldsymbol{p}$ can be determined for a known state of deformation $\boldsymbol{x}(t)$ and for a given membrane constitutive law. The capillary number ϵ in (2.7):

$$\epsilon = \mu V_0 / E_s,$$

is a measure of the deformability of the membrane in terms of the ratio between viscous stresses and elastic forces. As ϵ decreases, the membrane becomes stiffer or the forces

exerted by the fluids on the capsule decrease. Attention is drawn to the definition of ϵ when a constant-pressure-drop system is modelled: although the far-field velocity changes with $Q(t)$, the velocities are still scaled by V_0 which corresponds to $Q(0)$. The value of ϵ is thereby kept constant. If the velocities were scaled according to the current flow rate, ϵ would correspondingly vary, but the non-dimensional far-field velocity of the flow and therefore the non-dimensional flow rate would remain constant.

2.2. *Boundary integral formulation*

A convenient formulation of the problem is obtained by the boundary integral method. The integral equation expressing the velocity of points of M, B, S_i and S_o as a function of the velocities and forces on these surfaces is obtained following the same steps as Martinez & Udell (1990). We find that at time t, the velocity of a point on the membrane is given by

$$\forall \boldsymbol{x} \in M,$$

$$\tfrac{1}{2}(\lambda+1)\,\boldsymbol{v}(\boldsymbol{x}) = -\int_{\partial\Omega} [\boldsymbol{K}(\boldsymbol{x}-\boldsymbol{y})\cdot\boldsymbol{v}(\boldsymbol{y})]\cdot\boldsymbol{n}(\boldsymbol{y})\,\mathrm{d}S(\boldsymbol{y}) - \frac{1}{8\pi}\int_{\partial\Omega} \boldsymbol{J}(\boldsymbol{x}-\boldsymbol{y})\cdot[\boldsymbol{\sigma}^{ext}(\boldsymbol{y})\cdot\boldsymbol{n}(\boldsymbol{y})]\,\mathrm{d}S(\boldsymbol{y})$$

$$+(\lambda-1)\,\mathrm{PV}\int_M [\boldsymbol{K}(\boldsymbol{x}-\boldsymbol{y})\cdot\boldsymbol{v}(\boldsymbol{y})]\cdot\boldsymbol{n}(\boldsymbol{y})\,\mathrm{d}S(\boldsymbol{y}) + \frac{1}{8\pi}\int_M \boldsymbol{J}(\boldsymbol{x}-\boldsymbol{y})\cdot\frac{\boldsymbol{p}(\boldsymbol{y})}{\epsilon}\,\mathrm{d}S(\boldsymbol{y}), \quad (2.8)$$

where $\partial\Omega = B \cup S_i \cup S_o$. The Principal Value of the double-layer potential when $\boldsymbol{x}$ is on M, is denoted PV. On B, the scalar product $-[\boldsymbol{\sigma}^{ext}(\boldsymbol{y})\cdot\boldsymbol{n}(\boldsymbol{y})]$ is the force exerted by B on the fluid. On S_i or S_o, $\boldsymbol{\sigma}^{ext}$ is $-P_i\boldsymbol{I}$ or $-P_o\boldsymbol{I}$. The kernels $\boldsymbol{K}$ and $\boldsymbol{J}$ are known functions of position given by

$$J_{ij}(r) = \frac{\delta_{ij}}{|\boldsymbol{r}|} + \frac{r_i r_j}{|\boldsymbol{r}|^3}, \quad K_{ijk}(r) = \frac{-3}{4\pi}\frac{r_i r_j r_k}{|\boldsymbol{r}|^5},$$

where $\boldsymbol{r} = \boldsymbol{x}-\boldsymbol{y}$.

For points $\boldsymbol{x}$ on $\partial\Omega$, another integral equation similar to (2.8) is obtained. When the internal and external fluid viscosities are equal, λ is unity, and the double-layer potential vanishes on M. This is the case that is treated here and from now on, λ will be set to 1.

It is convenient to use perturbation quantities defined as the difference between the value of a variable in the presence of the capsule and the corresponding value without the capsule. Another integral equation is then obtained, that is valid for any point $\boldsymbol{x}$ on M or on $\partial\Omega$:

$$\forall \boldsymbol{x} \in M \cup \partial\Omega,$$

$$\frac{\boldsymbol{v}(\boldsymbol{x})-\boldsymbol{v}^{np}(\boldsymbol{x})}{\alpha} = -\int_{\partial\Omega} [\boldsymbol{K}(\boldsymbol{x}-\boldsymbol{y})\cdot\{\boldsymbol{v}(\boldsymbol{y})-\boldsymbol{v}^{np}(\boldsymbol{y})\}]\cdot\boldsymbol{n}(\boldsymbol{y})\,\mathrm{d}S(\boldsymbol{y})$$

$$+\frac{1}{8\pi}\int_M \boldsymbol{J}(\boldsymbol{x}-\boldsymbol{y})\cdot\frac{\boldsymbol{p}(\boldsymbol{y})}{\epsilon}\,\mathrm{d}S(\boldsymbol{y})$$

$$+\frac{1}{8\pi}\left\{\int_B \boldsymbol{J}(\boldsymbol{x}-\boldsymbol{y})\cdot\boldsymbol{f}_b^1(\boldsymbol{y})\,\mathrm{d}S(\boldsymbol{y})\right.$$

$$+\int_{S_i} \boldsymbol{J}(\boldsymbol{x}-\boldsymbol{y})\cdot(\Delta P_i\,\boldsymbol{e}_x)\,\mathrm{d}S(\boldsymbol{y})$$

$$\left.-\int_{S_o} \boldsymbol{J}(\boldsymbol{x}-\boldsymbol{y})\cdot(\Delta P_o\,\boldsymbol{e}_x)\,\mathrm{d}S(\boldsymbol{y})\right\}, \quad (2.9)$$

where the double-layer integral must be taken in the sense of its Principal Value when $\boldsymbol{x}$ is on $\partial\Omega$. The perturbation of the force exerted by B on the fluid is denoted $\boldsymbol{f}_b^1$, the axial unit vector is $\boldsymbol{e}_x$, and the pressure perturbations at the entrance and exit sections are respectively ΔP_i and ΔP_o. The parameter α is unity when $\boldsymbol{x}$ is on M, and is equal to 2 when $\boldsymbol{x}$ is on $\partial\Omega$. The velocity perturbation is at most $O(d^{-2}L^{-2})$ on S_i and S_o, where d is the minimum of the distance between a capsule point and the entrance and exit sections ($d \gg 1$ for (2.4) to be satisfied). Since the area of S_i and S_o is $O(L^2)$, the $\boldsymbol{K}$-integral in (2.9) can be neglected on S_i and S_o, and is exactly zero on B, according to (2.5). The advantage of using perturbation quantities is thus that it is possible to neglect the double-layer potential contribution.

Since the flow is axisymmetric, the ϕ-dependency can be integrated analytically (Youngren & Acrivos 1975), further reducing the dimension of the problem and converting the surface integrals into line integrals along a meridian curve with arclength denoted s_B on B, s_M on M and r on the normal sections S_i and S_o. The final equations are then

$\forall \boldsymbol{x} \in M, B, S_i$ or S_o:

$$\frac{1}{\alpha}\begin{bmatrix} v_x(\boldsymbol{x}) \\ v_r(\boldsymbol{x}) \end{bmatrix} = \frac{1}{\alpha}\begin{bmatrix} v_x^{np}(\boldsymbol{x}) \\ v_r^{np}(\boldsymbol{x}) \end{bmatrix} + \frac{1}{8\pi}\left\{ \int_{L_B} \begin{bmatrix} J_{xx}(\boldsymbol{x}-\boldsymbol{y}_B) & J_{xr} \\ J_{rx} & J_{rr} \end{bmatrix} \begin{bmatrix} f_{bx}^1(\boldsymbol{y}_B) \\ f_{br}^1(\boldsymbol{y}_B) \end{bmatrix} \mathrm{d}s_B \right.$$

$$+ \int_0^{r_i} \begin{bmatrix} J_{xx}(\boldsymbol{x}-\boldsymbol{y}_{s_i}) & J_{xr} \\ J_{rx} & J_{rr} \end{bmatrix} \begin{bmatrix} \Delta P_i \\ 0 \end{bmatrix} \mathrm{d}r - \int_0^{r_o} \begin{bmatrix} J_{xx}(\boldsymbol{x}-\boldsymbol{y}_{s_o}) & J_{xr} \\ J_{rx} & J_{rr} \end{bmatrix} \begin{bmatrix} \Delta P_o \\ 0 \end{bmatrix} \mathrm{d}r$$

$$\left. + \frac{1}{c}\int_{L_M} \begin{bmatrix} J_{xx}(\boldsymbol{x}-\boldsymbol{y}_M) & J_{xr} \\ J_{rx} & J_{rr} \end{bmatrix} \begin{bmatrix} p_x(\boldsymbol{y}_M) \\ p_r(\boldsymbol{y}_M) \end{bmatrix} \mathrm{d}s_M \right\}, \tag{2.10}$$

where L_B and L_M are respectively the meridian curves of B and M, and where r_i and r_o are the radii of the constriction in the entrance and exit sections. The kernels $\boldsymbol{J}$ can be found in Li *et al.* (1988) or in Pozrikidis (1992). Although the integrals in (2.10) are improper when $\boldsymbol{y} = \boldsymbol{x}$, owing to the singular behaviour of the kernels $\boldsymbol{J}$, they may be shown to converge because of the logarithmic behaviour of the singularity.

2.3. *Capsule membrane mechanics*

The membrane deformation is expressed in terms of Lagrangian variables by labelling the membrane material points along a meridian curve by their coordinates ξ, ρ, and arclength S ($S = 0$ at the first upstream point of the membrane where $\rho = 0$) before deformation. After deformation, the points have coordinates x, r and arclength s ($s = 0$ where $S = 0$). The membrane equations greatly simplify since the principal directions of strain and stress at each point are along the meridian and azimuthal directions. The deformation is therefore expressed in terms of the principal extension ratios λ_s and λ_ϕ in these directions, defined as

$$\lambda_s = \mathrm{d}s/\mathrm{d}S; \quad \lambda_\phi = r/\rho. \tag{2.11a, b}$$

Any type of hyperelastic behaviour may be chosen for the membrane, but the results presented in this paper focus on the case of an infinitely thin membrane with a Mooney–Rivlin law. The principal elastic tensions per unit length are deduced from the classical theory of shell mechanics (Green & Adkins 1960; Barthes-Biesel & Rallison 1981) and, in the particular case of a neo-Hookean material, are given by

$$T_s = \frac{1}{3\lambda_s\lambda_\phi}\left(\lambda_s^2 - \frac{1}{\lambda_s^2\lambda_\phi^2}\right), \quad T_\phi = \frac{1}{3\lambda_s\lambda_\phi}\left(\lambda_\phi^2 - \frac{1}{\lambda_s^2\lambda_\phi^2}\right). \tag{2.12a, b}$$

The shell equilibrium equations give the tangential and normal components of the force $\boldsymbol{p}$ exerted by the membrane:

$$p_s = \frac{\mathrm{d}T_s}{\mathrm{d}s} + \frac{1}{r}\frac{\mathrm{d}r}{\mathrm{d}s}(T_s - T_\phi) = \boldsymbol{p}\cdot\boldsymbol{\tau}, \quad p_n = -(K_s T_s + K_\phi T_\phi) = \boldsymbol{p}\cdot\boldsymbol{n}, \qquad (2.13a, b)$$

where $\boldsymbol{\tau}$ is the unit tangent vector to the meridian, oriented in the direction of increasing S and where K_s and K_ϕ are the principal curvatures of M:

$$K_s = -\left(\frac{\mathrm{d}\tau_x}{\mathrm{d}s}n_x + \frac{\mathrm{d}\tau_r}{\mathrm{d}s}n_r\right), \quad K_\phi = \frac{n_r}{r}. \qquad (2.14a, b)$$

The components of $\boldsymbol{p}$ in cylindrical coordinates are easily deduced.

The problem is thus reduced to solving equation (2.10) with boundary conditions (2.4)–(2.7). The integration of the kinematic condition (2.6) gives the instantaneous position of the membrane points, and the force $\boldsymbol{p}$ is obtained from (2.11)–(2.14).

3. Numerical procedure

The general objective of this model is to simulate the passage of a capsule through a hyperbolic constriction under either a constant pressure drop or a constant flow rate until it either plugs the constriction or reaches a chosen position downstream the throat. A collocation technique is used, based on a discretization of the boundaries, followed by the determination of either the unknown forces or unknown velocity at discrete locations. The undeformed meridian curve of M is partitioned by n_M points $x_1, \ldots, x_{n_M}$ evenly spaced along the arclength. The meridian curve of B is discretized into n_B points, equally spaced along the parameter $\mathrm{Arch}(r_b)$, where r_b is the radial coordinate of a point on B. The point density on B is therefore higher in the region of high curvature, near the throat of the constriction. Sections S_i and S_o are uniformly partitioned into n_S points.

The singularities of the kernels $\boldsymbol{J}$ are treated by subtracting the asymptotic expression $\boldsymbol{J}^*$ of the singular terms and then adding the analytically calculated sum (Li *et al.*). The singular integrals of the single-layer potentials on M, B, S_i and S_o then become

$$\int_{L_s} \boldsymbol{J}(\boldsymbol{x}_j - \boldsymbol{y})\cdot\boldsymbol{f}(\boldsymbol{y})\,\mathrm{d}s(\boldsymbol{y}) = \sum_{i=1}^{N} w_s(\boldsymbol{x}_i)[\boldsymbol{J}(\boldsymbol{x}_j - \boldsymbol{x}_i)\cdot\boldsymbol{f}(\boldsymbol{x}_i) - \boldsymbol{J}^*(\boldsymbol{x}_j - \boldsymbol{x}_i)\cdot\boldsymbol{f}(\boldsymbol{x}_j)]$$

$$+\boldsymbol{f}(\boldsymbol{x}_j)\cdot\int_{L_s}\boldsymbol{J}^*(\boldsymbol{x}_j - \boldsymbol{y})\,\mathrm{d}s(\boldsymbol{y}), \quad j = 1, N,$$

where L_s represents any boundary partitioned with N collocation points. When $i = j$, the corresponding term in the sum is exactly zero. The expressions for $\boldsymbol{J}^*$ are given by Li *et al.* for $\boldsymbol{x}$ and $\boldsymbol{y}$ on M. Similar expressions can easily be derived for $\boldsymbol{x}$ and $\boldsymbol{y}$ on $\partial\Omega$. The numerical integrations are performed by means of Simpson's rule adapted for uneven intervals, with accuracy of order Δs^4, where Δs represents the maximum interval length. The corresponding weights w_s depend on the collocation point spacing only.

At time $t = 0$, the undeformed capsule is introduced into the flow at a position measured by the distance $|x_G(0)|$ between its centre of mass and the origin O of the

reference frame. At time t, the position of the membrane collocation points is known, and the local tangent and normal vectors, as well as the curvature of the meridian line, are obtained directly by numerical derivations performed with the five-unequally-spaced-point scheme used by Li *et al.* (with an accuracy of order Δs^2 for the second derivative). The computation of the azimuthal curvature K_ϕ and extension ratio λ_ϕ present no difficulty except for the points x_{n_M} and x_1 where they are set equal to the meridian curvature K_s and extension ratio λ_s, respectively. The value of the force $\boldsymbol{p}$ follows readily from (2.13*a*, *b*).

Equation (2.10) where $\alpha = 2$ is then used to determine $\boldsymbol{f}_b^1$ at every collocation point on B, together with ΔP_i and ΔP_o. A linear system consisting of $2n_B+2$ scalar equations for the $2n_B+2$ unknowns (n_B values of f_{bx}^1 and f_{br}^1, plus ΔP_i and ΔP_o) is then solved.

In the case of constant flow rate, $\boldsymbol{p}$, $\boldsymbol{f}_b^1$, ΔP_i and ΔP_o are directly introduced in equation (2.10) with $\alpha = 1$ to compute the velocity $\boldsymbol{v}_i$ of the membrane points $\boldsymbol{x}_i$ for $i = 1, \ldots, n_M$. In the case of constant pressure drop, it is first necessary to determine the flow rate $Q(t)$ by means of (2.2), where $\Delta P_{add}(t)$ is simply $\Delta P_i - \Delta P_o$. The unperturbed flow field $\boldsymbol{v}^{np}(t)$ at time t follows readily and (2.10) can then be used as described above. Once the velocity of the membrane points at time t is determined, their new position at time $t+\Delta t$ is computed by integrating the kinematic condition (2.6) by means of an Eulerian explicit scheme:

$$\boldsymbol{x}_i(t+\Delta t) = \boldsymbol{x}_i(t) + \boldsymbol{v}_i(t)\,\Delta t, \quad \boldsymbol{v}_i(t=0) = \boldsymbol{v}_i^{np}(t=0).$$

The process is initiated at time $t = 0$ by assigning the unperturbed velocity of the flow to all the membrane points, and is stopped either when the capsule centre of mass has reached a specified position downstream of the constriction, or when plugging is detected. Plugging is considered to occur when the membrane tends to touch the wall. It is then necessary to stop the calculation for two reasons: contact forces between the membrane and the wall are not accounted for, and new singularities appear in boundary integrals that were otherwise non-singular. The plugging criterion is based on the minimum gap width between the membrane and the channel wall being larger than 0.01.

The computation of the membrane deformation and load $\boldsymbol{p}$ requires two successive numerical derivations of the instantaneous position of the membrane points. Correspondingly, as was observed by Rallison & Acrivos, by Li *et al.* and by Pozrikidis, the computed extension ratios λ_s, λ_ϕ and elastic tensions T_s, T_ϕ exhibit an oscillation with a period equal to twice the collocation-point spacing. An increase in the collocation-point density alleviates the problem but leads to prohibitively large computation times. As first suggested by Li *et al.*, another way to alleviate the problem is to perform a numerical smoothing of the deformed profile. Pozrikidis has shown that the smoothing method proposed by Longuet-Higgins & Cokelet (1976) is stable and efficient for this type of problem. Only the profiles (here the membrane point coordinates x and r) need be smoothed for all the other variables to behave smoothly.

The volume conservation of the capsule is implicitly guaranteed by the Stokes equations. However, numerical errors lead to small volume variations at each time step (less than 10^{-6} in the present results). If no particular precautions are taken, after a large number of time iterations (typically of order 250000), the accumulation of numerical errors may lead to volume variations of order 5% to 15% in extreme cases near plugging. This classical problem experienced by other authors (Martinez & Udell) is solved by correcting the volume periodically. The positions of the capsule points with respect to the centre of mass are thus rescaled by a factor equal to the cube root of the volume, at each time step.

The explicit character of the solution scheme (Eulerian time integration scheme) makes it susceptible to numerical instability. Li *et al.* have introduced the following stability criterion:

$$\Delta t < \epsilon \Delta s$$

which obviously leads to very small values of Δt, especially where numerical precision requires that Δs be small.

Numerical validation of the model

The validation of the model is difficult owing to the time-dependent nature of the problem and to the absence of either analytical or numerical solutions. An additional difficulty comes from the fact that all parameters influencing the accuracy of the model are interrelated in the way they affect the convergence of the scheme. For lack of a better alternative, the scheme will be said to converge when any significant change (over 50%) of one or more numerical parameters (density of collocation points on the boundaries, Δt) and/or physical parameters (position of S_i and S_o, $x_G(0)$) produces a change of no more than 5% in a selected control variable, i.e. the flow rate or the additional pressure drop. This leads to the determination of acceptable values of these parameters, based on the balance between the need for numerical precision and the necessity to restrain computational cost. As an additional check, at each time step the force balance was verified over a control volume delimited by S_i, S_o and B. An order of accuracy to the eighth decimal place was obtained for each iteration in all the results presented here.

The value of L must be such that P_i and P_o be uniform and (2.4) satisfied within a good approximation. Acceptable values of $x_G(0)$ and of L are thus closely related. For capsules tested here, it was found that a ratio $L/|x_G(0)|$ of order 5 was acceptable to satisfy (2.4). Then the largest $|x_G(0)|$ for which the model converged was determined. This value depends both on the size ratio and on ϵ. Typically, the values of L and $x_G(0)$ were respectively of order 35 and -7.

A sensitive parameter for the solution of (2.10) in terms of the forces on B, S_i and S_o, is the density of points on these boundaries. As shown by Delves & Mohamed (1985), the Nystrom method used here is better adapted to Fredholm equations of the second kind. In the case of Fredholm equations of the first kind, as in this model, the efficiency of this solution technique may decrease as the partition of the boundaries is made finer. It is therefore necessary to prove that the range in which parameters n_B and n_S are chosen is safe. Some numerical tests are presented for constant-pressure-drop conditions, for a capsule that is 40% larger than the throat ($R = 1.4$) and a capillary number set to $\epsilon = 1$. The flow rate Q in the channel is shown as a function of the position of the capsule centre of mass along the axis. Such a graph is shown here for numerical validation purposes and is commented upon in §4. The mesh size on the entrance and exit sections is first set to 0.25. A comparison of the results obtained when B is partitioned with $n_B = 241, 375, 481$ points, is shown on figure 2. The corresponding values of the minimum flow rate are respectively 2.538, 2.555 and 2.561. Consequently, when n_B is increased from 375 to 481, the results are superimposed within graphical accuracy. When the mesh size on S_i and S_o is divided by 2, the results differ by less than 0.1%.

For a given value of ϵ, once a safe value of Δt has been determined, n_M can be increased (and Δt proportionally decreased) until the evolution of the flow rate or pressure perturbation is not affected anymore. Results obtained with two different mesh sizes on the undeformed capsule $\Delta S = 7 \times 10^{-2}$ and 3.5×10^{-2}, with an associated time step $\Delta t = 1 \times 10^{-3}$ and 0.5×10^{-3}, differ by no more than 0.3%.

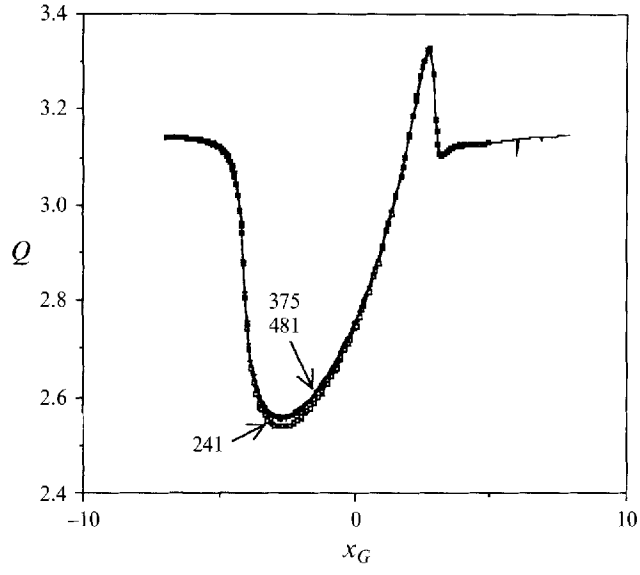

FIGURE 2. Evolution of volume flow rate Q as a function of centre of mass position x_G. Case $R = 1.4$, $\epsilon = 1$. The channel boundary is partitioned with 241, 375 or 481 collocation points. The results obtained with the last two partitions are superimposed within graphical precision.

The effect of the smoothing procedure was evaluated by comparing the results obtained with ($\Delta S = 7 \times 10^{-2}$, $\Delta t = 1 \times 10^{-3}$) and without smoothing, keeping the partitions of B, S_i and S_o unchanged and choosing a fine partition for M ($\Delta S = 3.5 \times 10^{-2}$, $\Delta t = 0.5 \times 10^{-3}$). The results obtained for the flow rate differ by less than 0.8%. This indicates that smoothing does not significantly perturb the results, while it allows us to use a larger mesh size and thus to reduce significantly the CPU time.

Finally, to check the accuracy of the Eulerian time integration scheme, the time step was decreased by a factor of 2 with all the other parameters kept the same. The results were found to differ by less than 0.3% for both the capsule shape and the evolution of the flow rate.

4. Constant pressure drop

When filtration is used to determine the mechanical properties of cells or capsules, the pore size is usually chosen to be slightly smaller than the resting size of the particles so that the membrane is subjected to sufficient mechanical forces. The initially spherical capsules studied in this first set of numerical experiments have size ratios R larger than unity, and the opening of the constriction throat is set to $\zeta_0 = 0.7$ in all cases. As ζ_0 varies between 0 and 0.7, the hydraulic resistance increases from 3 to 5. Consequently, a value of ζ_0 less than 0.7 is not expected to produce significantly different results. For values of ζ_0 larger than 0.7, the constriction becomes very gradual and thus does not represent well a pore entrance. Furthermore, the hydraulic resistance measured experimentally by Drochon (1991) for the pore of filters used for blood cell filtration, corresponds to the sum of the resistance of a short cylinder (corresponding to the pore itself) and of a hyperbolic constriction with $\zeta_0 = 0.7$. The flow is driven by a constant pressure drop.

A typical case where $R = 1.4$ and $\epsilon = 0.3$, corresponding to a capsule that is

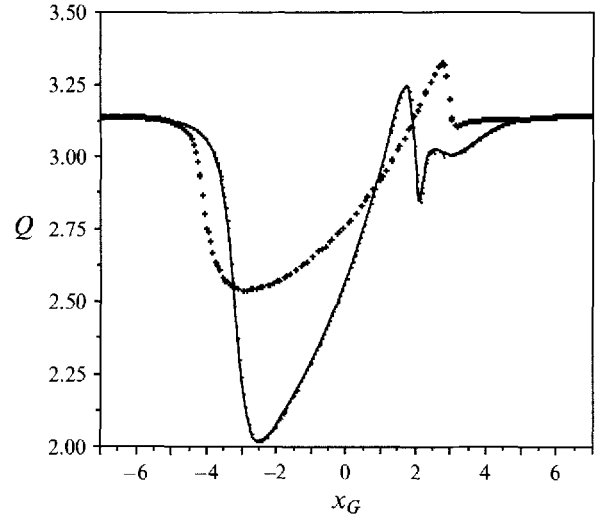

FIGURE 3. Evolution of volume flow rate Q as a function of centre of mass position x_G for $\epsilon = 0.3$ (—●—) and $\epsilon = 1$ (+).

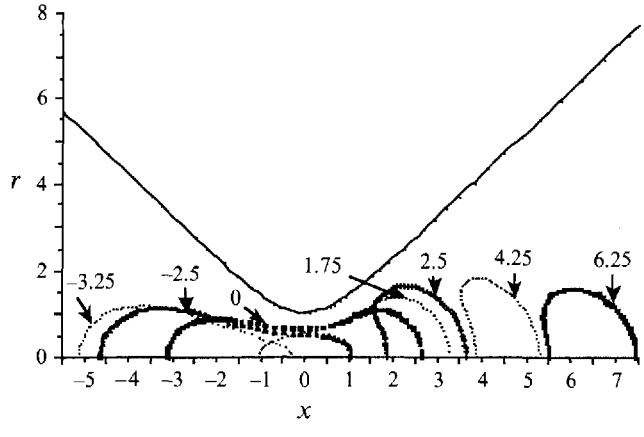

FIGURE 4. Successive profiles of a capsule with initial radius $R = 1.4$ at $\epsilon = 0.3$, for different positions of the centre of mass x_G, as indicated on the figure.

deformable enough to go through the constriction without touching the walls, is discussed in detail. The role of the capillary number is studied by comparing two cases where $\epsilon = 1$ and 0.3. Then, the influence of the size ratio is evaluated by comparing the flow rate evolution in three cases ($R = 1.2$, 1.4 and 1.8) when $\epsilon = 0.3$. Pore plugging is investigated through the study of $R = 1.8$ at $\epsilon = 0.05$ and $R = 1.4$ at $\epsilon = 0.03$.

4.1. *Characteristic motion of non-plugging capsules* ($R = 1.4$, $\epsilon = 0.3$)

The capsule starts from the position $x_G(0) = -7$ determined as explained earlier. The entrance and exit sections are located at a distance $L = 35$ from the constriction throat. The evolution of the flow rate Q as a function of the instantaneous capsule centre of mass position x_G is shown on figure 3. The deformed profiles are shown on figure 4 for capsule positions $x_G = -3.25$, -2.5, 0.0, 1.75, 2.5, 4.25, 6.25. The variation with S of

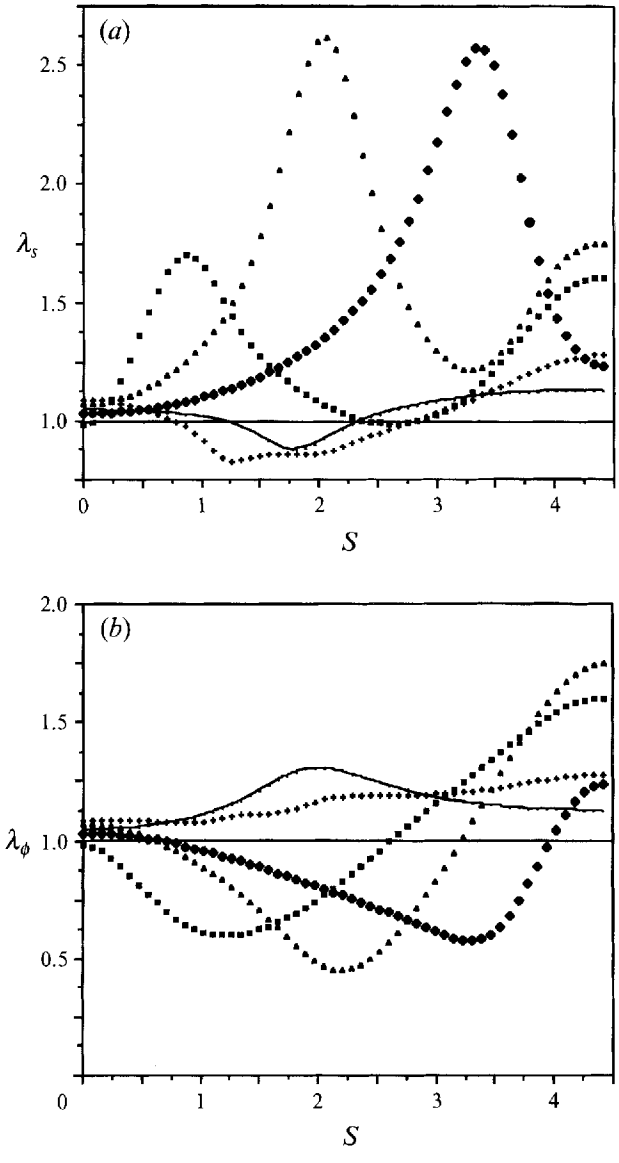

FIGURE 5. Evolution of the longitudinal $\lambda_s(a)$ and hoop $\lambda_\phi(b)$ extension ratios as a function of the initial arclength S for $R = 1.4$ and $\epsilon = 0.3$, for significant positions of the centre of mass: ◆, $x_G = -2.5$; ▲, $x_G = 0$; ■, $x_G = 1.75$; +, $x_G = 2.5$; —●—, $x_G = 4.25$.

the meridional λ_s and hoop λ_ϕ extension ratios, and of the meridional T_s and hoop T_ϕ elastic tensions in the membrane are shown respectively in figures 5(*a*, *b*) and 6(*a*, *b*). The net resultant force exerted by the membrane on the fluids vanishes since the system is inertialess. However, the rate of energy $\dot{W}$ exchanged between the membrane and the fluids is finite:

$$\dot{W} = \frac{1}{\epsilon}\int_M \boldsymbol{p}\cdot\boldsymbol{v}\,\mathrm{d}S,$$

and provides information on the relationship between membrane micromechanics and bulk flow variations. The evolution of $\dot{W}$ with x_G is shown on figure 7. When $\dot{W}$ is

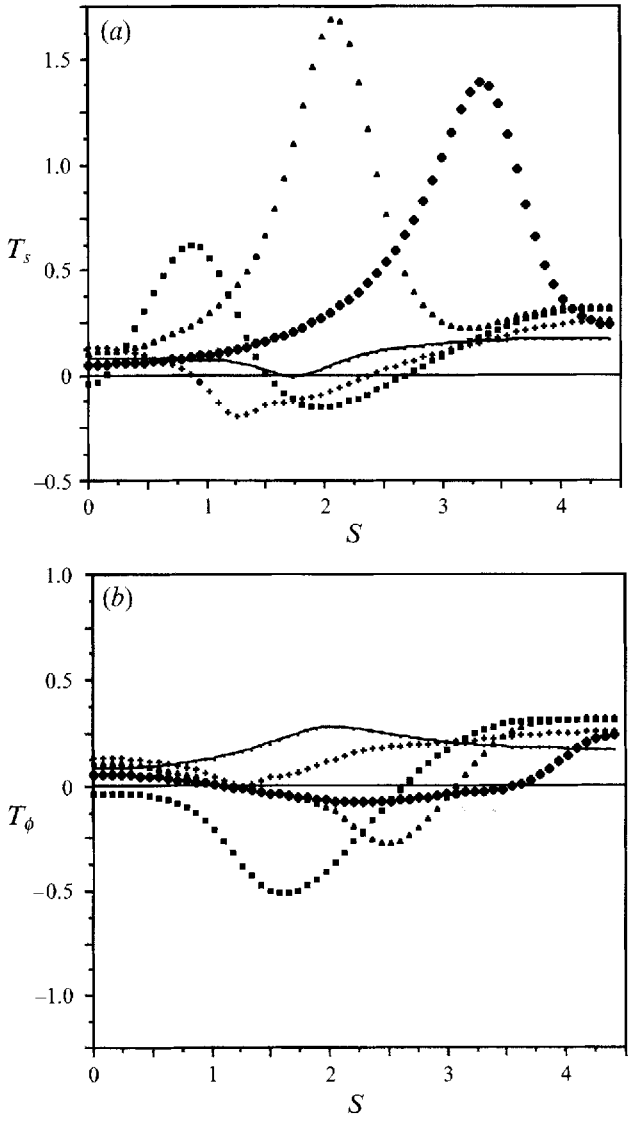

FIGURE 6. Evolution of the longitudinal $T_s(a)$ and hoop $T_\phi(b)$ elastic tensions as a function of the initial arclength S for $R = 1.4$ and $\epsilon = 0.3$, for significant positions of the centre of mass: ◆, $x_G = -2.5$; ▲, $x_G = 0$; ■, $x_G = 1.75$; +, $x_G = 2.5$; —●—, $x_G = 4.25$.

negative, the membrane energy consumption increases. When it is positive, the membrane tends to restore energy to the system.

It should be kept in mind that the flow accelerates upstream of the throat and then decelerates, so that the problem is transient owing to both geometric and kinematic reasons. Correspondingly, the capsule motion and deformation proceed roughly in three phases: a suction phase where the front of the capsule is pulled into the pore (Q decreases), a transit phase where the front of the capsule has reached the decelerating region while the rear is still accelerating (Q increases), and finally a recoil phase where the capsule returns to its equilibrium shape (Q oscillates back to the initial value π). In the following, each phase is specified by a range of values of x_G, the bounds of which should not be interpreted in a precise sense.

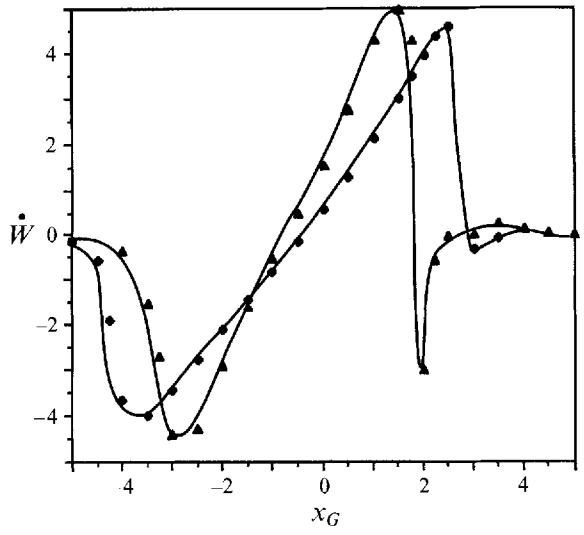

FIGURE 7. Evolution of the rate of energy $\dot{W}$ exchanged between the membrane and the fluids as a function of centre of mass position x_G for $R = 1.4$, and two capillary numbers: ▲, $\epsilon = 0.3$; ◆, $\epsilon = 1$.

(i) Suction phase: $x_G < -2.5$

The capsule is stretched along the meridian. Its front being subjected to increasing levels of velocity, it extends rapidly, as can be readily surmized from the evolution of λ_s (figure 5*a*). As the capsule moves into the constriction, the peak in meridional extension becomes larger and is concurrently shifted towards the middle of the particle. Quite large extension ratios are attained ($\lambda_s \approx 2.6$). The elastic tension T_s is positive, and its evolution follows that of λ_s. The hoop extension ratio and tension values are much smaller than the corresponding meridional ones. This indicates that in the region of maximum extension, the parallel curves are compressed. Since $\dot{W}$ is negative, the membrane deformation consumes an increasing amount of energy and the flow is consequently retarded. The minimum of $\dot{W}$ corresponds to the minimum of Q.

(ii) Transit phase: $-2.5 < x_G < 1$

The front part of the capsule has passed through the constriction and is slowing down. The front meridional extension would tend to decrease, but the nose of the capsule expands radially, leading to values of the hoop tension and extension ratio larger than in the suction phase (figures 5*a*, *b* and 6*a*, *b*). The portion of capsule located at the throat is still under tension and undergoes large deformations ($\max(\lambda_s) \approx 2.6$ for $x_G = 0$), the level of which decreases after the capsule centre of mass has passed the throat ($x_G > 0$). Owing to elastic energy recovery between the rear and the front of the capsule, $\dot{W}$ increases from negative to positive values. The position of x_G where $\dot{W}$ becomes positive corresponds to the point where the maximum level of T_s along the capsule meridian starts decreasing (figure 6*a*). This indicates that the capsule restores elastic energy to the system.

(iii) Recoil phase: $x_G > 1$

In this phase, the cooperative effect of the elastic forces causes values of Q to become larger than that at the initial level. The front of the capsule has virtually stopped, while the rear still has a substantial velocity, and thus tends to re-enter the capsule, leading

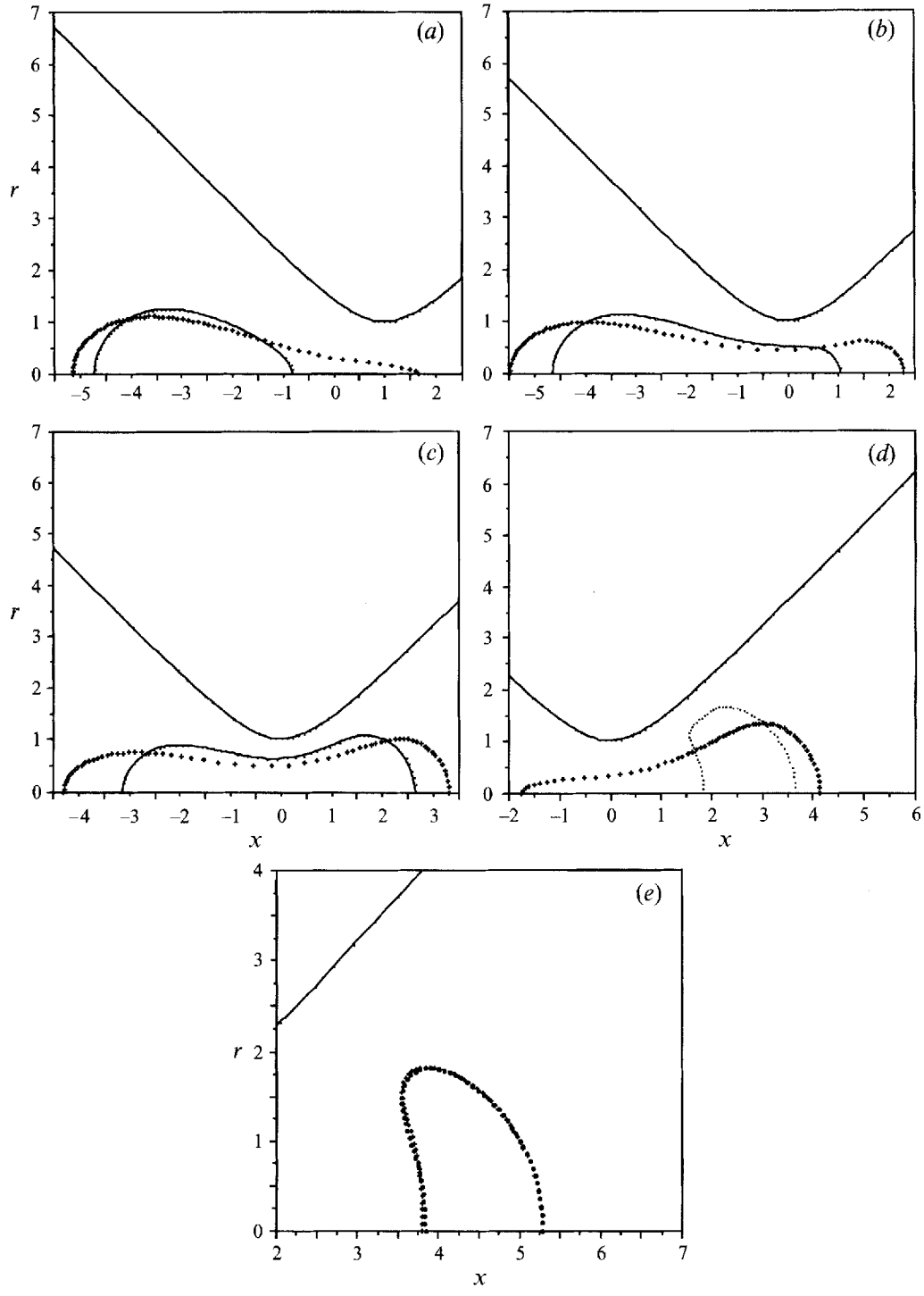

FIGURE 8. Comparison of the deformed profiles of two capsules of initial radius $R = 1.4$ for two capillary numbers: ●, $\epsilon = 0.3$; +, $\epsilon = 1$. (*a*) $x_G = -4$, (*b*) $x_G = -2.5$, (*c*) $x_G = 0$, (*d*) $x_G = 2.5$, (*e*) $x_G = 4.25$.

to a 'parachute' shape. The front of the capsule is under tension in both the meridional and hoop directions. The recoil phase begins when the meridional tension T_s becomes negative and pulls the downstream part of the capsule. Correspondingly, the extension ratio λ_s decreases (compare for example the values of λ_s for $x_G = 1.75$ and 2.5 on figure 5*a*), and may become slightly smaller than unity in some parts of the membrane. At $x_G = 1.75$ (corresponding to the maximum value of the flow rate), $\dot{W}$ and Q start decreasing again, owing to the elastic forces that tend to compress the interface (T_s becomes negative in some parts) even though the membrane resists this type of deformation. The front of the capsule then expands radially, thus relieving compression. This leads again to cooperative elastic forces and to an increase in $\dot{W}$ and Q. The parachute shape fades away and the flow rate eventually returns to its original value as the capsule regains a spherical shape. The oscillations of the flow rate are therefore related to the successive phases of extension/compression of the capsule membrane.

Although some parts of the membrane appear to be slightly under compression ($\lambda_s < 1$), no buckling is observed. In real situations, the bending rigidity of the interface, however small, would prevent buckling. As was pointed out by Pozrikidis (1990), the numerical smoothing of the deformed profiles may play a role that is qualitatively similar to that of bending resistance. Also, the overall behaviour of the capsule indicates no tendency to breakup through a process of continuing extension, as happens in elongational flows (Li *et al.*). This is due to the specific configuration of the flow, where the deceleration phase following the constriction stops the particle and allows the elastic forces to operate. For very deformable capsules, the high deformation levels reached in the flow process might lead to breakup due to material failure. It is interesting that the parachute shape is similar to that observed when red blood cells flow through narrow capillaries, even though the present capsules are initially spherical. Here, this shape is produced by the negative downstream velocity gradient.

4.2. *Effect of the capillary number and capsule radius*

(i) Effect of the capillary number: $R = 1.4$, $\epsilon = 0.3$ and $\epsilon = 1$

The phenomena observed when the capillary number is greater than 0.3 are qualitatively similar to those described above, as far as the evolution of the capsule shape, of $\dot{W}$ and Q is concerned. The effect of ϵ can be assessed by comparing two capsules $C_{0.3}$ and C_1 of same initial radius ($R = 1.4$) with respectively $\epsilon = 0.3$ and $\epsilon = 1$ (figures 3 and 7). Capsule C_1 is more deformable than $C_{0.3}$, under identical flow conditions. The deformed profiles are compared on figure 8(*a–e*), for identical positions of the centres of mass.

An increase in ϵ leads to a decrease of the maximum flow perturbation ($\Delta Q_{max}/Q_0 = 20\%$ for C_1 and $\Delta Q_{max}/Q_0 = 36\%$ for $C_{0.3}$), and of the rate of energy consumption (figure 7). The deformation process starts further upstream of the throat for C_1, and the flow rate begins to decrease when x_G is still comparatively far from the throat. Correspondingly, the recoil phase occurs for values of x_G that are larger for C_1 than for $C_{0.3}$. Indeed, since the elastic tensions are small for C_1, they are not pulling the rear of the capsule efficiently. Correspondingly, the role of viscous forces in the recovery process is important for C_1, and the oscillations back to the initial state are damped out quickly. The deformation and relaxation processes thus take place over a larger length of the constriction as the capillary number is increased. This can be easily verified from a comparison of the deformed profiles of the two capsules (figures 8*a–e*).

A convenient way of depicting the global evolution of the capsule shape is to plot the axial positions of the capsule nose and tail as a function of x_G (figure 9). The

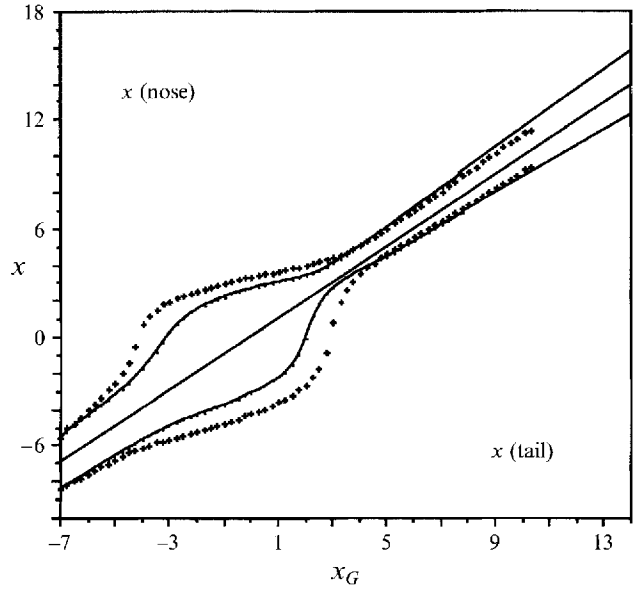

FIGURE 9. Evolution of the axial position of the nose, x(nose), and of the tail, x(tail), as a function of x_G: —●—, $C_{0.3}$; +, C_1.

parachute shapes are attained when the distance between the tail of the capsule and the centre of mass decreases, and thus when the x(tail) curve comes close to the straight line $x = x_G$. This position is reached closer to the throat for $C_{0.3}$ than for C_1. In fact, the stiffer the capsule (for a given flow velocity and liquid viscosity), the closer to the throat, on the downstream side, it will attain its sharpest parachute shape. Figure 9 allows the extrapolation of the position of x_G where the capsule regains a spherical shape.

In the limit of infinitely large values of ϵ, the interface is simply a collection of material points convected by the undisturbed flow field. Such a fictitious capsule would reach a parachute shape downstream of the throat and keep expanding in the radial direction, whereas, owing to the elasticity of their membrane, capsules with finite values of ϵ ultimately recover a spherical shape.

The evolution of the centre of mass velocity V_G is a complex function not only of x_G, but also of the state of deformation of the membrane, and thus of ϵ. Figure 10 shows the variations of V_G with x_G for the two capsules $C_{0.3}$ and C_1. For comparison, the initial undisturbed axial fluid velocity $v_0^{np}(x_G)$ at the same position x_G is also plotted. The velocity of C_1 deviates significantly from the unperturbed fluid velocity for $x_G > -5$. Before this point, the capsule is almost undeformed, and travels through the pore with roughly the initial unperturbed fluid velocity. For $-5 < x_G < -2.5$, V_G is larger than $v_0^{np}(x_G)$. Indeed, the front points of the capsule have reached the throat region where the velocities are large whereas the rear, which is almost undeformed, is still travelling with the unperturbed fluid velocity (figure 8*a*). The reason V_G becomes smaller than $v_0^{np}(x_G)$ for $x_G > -2.5$ is related to the significant decrease in flow rate and to the fact that the front points of the capsule have reached a decelerating region.

The effect of ϵ may be assessed by comparing the velocities V_{G1} and $V_{G0.3}$ of the two capsules C_1 and $C_{0.3}$. During the suction phase, V_{G1} is initially larger than $V_{G0.3}$. This is because the front part of C_1 is in a high-velocity region, while all of $C_{0.3}$ is still in a low-velocity region. However, during the transit phase, $V_{G0.3}$ becomes larger than V_{G1}:

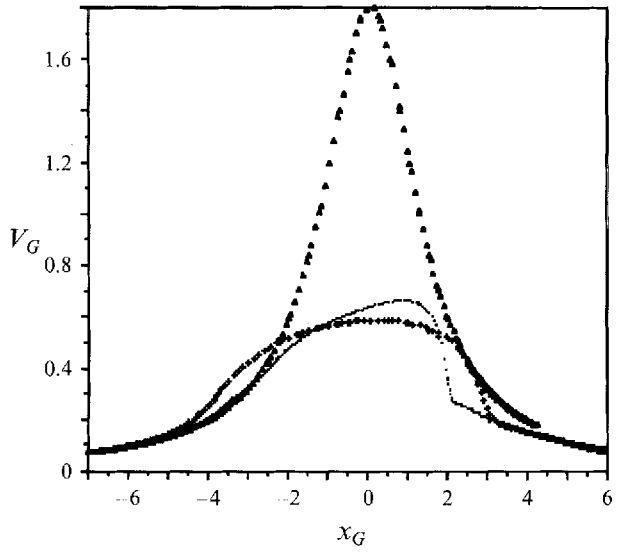

FIGURE 10. Evolution of the centre of mass velocity V_G of $C_{0.3}$ (●) and of C_1 (+). Comparison with the initial non-perturbed fluid velocity (▲).

although the flow rate decrease is larger for $C_{0.3}$, its deformation is smaller and it is globally closer to the throat than C_1. Larger values of V_{G1} are observed between $x_G = 1.75$ and 3 and may be attributed to the fact that, in this region of x_G, the flow rate at $\epsilon = 1$ becomes significantly larger than the flow rate at $\epsilon = 0.3$. Indeed, C_1 enters the early recoil phase where Q increases above π whereas $C_{0.3}$ is already in the phase where the flow rate oscillates below π. During the final phase of the recovery process the three velocity curves are superimposed. These results are useful for analysing filtration data, since they give information on the residence time of different capsules in a pore.

(ii) Effect of capsule size: $\epsilon = 0.3$, $R = 1.2$, 1.4 and 1.8

Figure 11 shows that for $\epsilon = 0.3$, capsules with size ratios up to 1.8 can go through the constriction and reach the downstream side of the throat without touching the walls. As expected, larger capsules start deforming further upstream of the throat than smaller capsules. As a consequence, the flow rate starts decreasing at $x_G = -6$, -5 or -4 respectively for $R = 1.8$, 1.4 or 1.2. Similarly, the transit phase begins for positions of x_G further upstream of throat for larger R ($x_G = -3$ for $R = 1.8$ versus $x_G = -2$ for $R = 1.2$), because larger capsules extend more readily and their nose reaches the throat for positions of their centre of mass still fairly far upstream in the constriction.

For a given position of x_G in the suction or transit phase, the larger the capsule, the larger the flow perturbation. When R is increased from 1.2 to 1.8, i.e. for a difference of 50% in the initial radius of the capsule, or, correspondingly, a difference of 240% in the initial volume of the capsule, the maximum flow rate perturbation $\Delta Q/Q_0$ changes from 30% to 44%. Although the transit phase is longer for larger capsules, the rate of increase of Q with x_G is roughly the same for all three initial radii. This confirms that this rate of increase is directly related to the membrane elasticity.

4.3. *Pore plugging*

Pore plugging is an experimental problem that occurs frequently when the pressure head is not high enough to force a given capsule through a pore. The occurrence of plugging then perturbs the filtration results considerably. It is thus important to be able

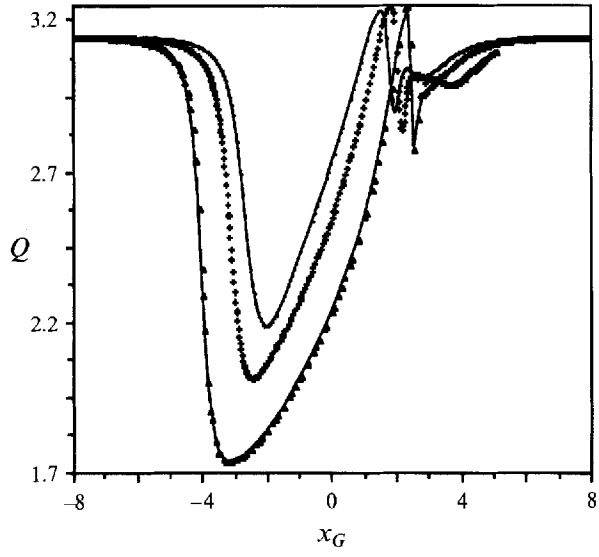

FIGURE 11. Evolution of volume flow rate Q as a function of x_G for $\epsilon = 0.3$: ●, $R = 1.2$; +, $R = 1.4$; ▲, $R = 1.8$.

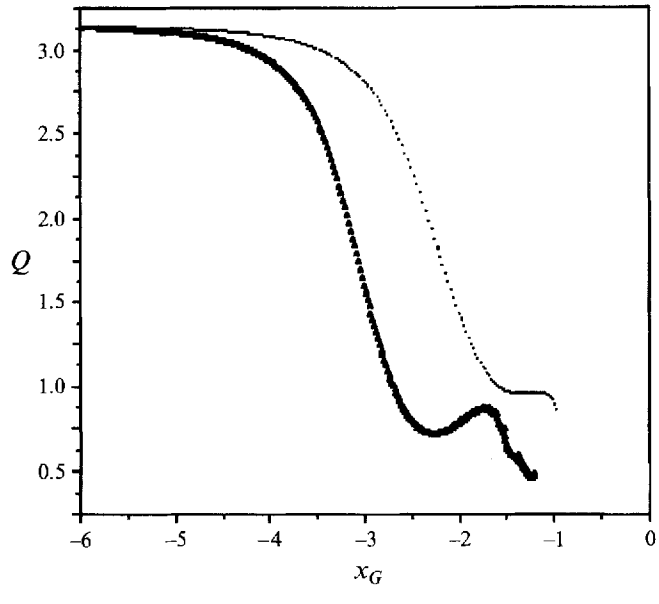

FIGURE 12. Evolution of volume flow rate Q as a function of x_G: ●, $R = 1.4$, $\epsilon = 0.03$; ▲, $R = 1.8$, $\epsilon = 0.05$.

to predict this phenomenon and to understand the prevailing physical mechanisms. Up to now, results have been presented for capsules deformable enough to go through the constriction. It is clear though, that very rigid or very large capsules would eventually block the pore. The numerical model predicts this occurrence. Indeed, it was found that in some cases, the capsule gets very near the wall of the constriction and that the flow rate then drops significantly. This is interpreted as plugging. It should be recognized though that, when membrane points touch the wall, the numerical model fails as explained in §3.

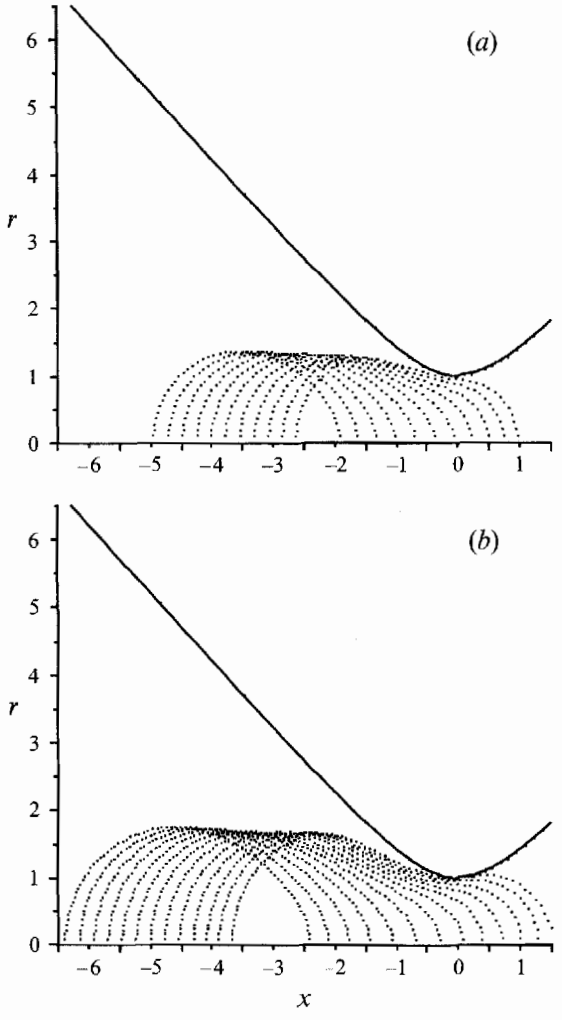

FIGURE 13. Successive profiles of a capsule showing plugging of the pore under constant pressure drop. (*a*) $R = 1.4$, $\epsilon = 0.03$; (*b*) $R = 1.8$, $\epsilon = 0.05$.

(i) Entry plugging

Figure 12 shows the evolution of the flow rate for two capsules ($R = 1.4$, $\epsilon = 0.03$ and $R = 1.8$, $\epsilon = 0.05$). In both cases, the suction phase is normal with the flow rate decreasing at a faster rate for the larger but more deformable capsule. However, when the nose of the capsule has passed the throat and when the transit phase should begin, the flow rate suddenly drops and tends to zero, indicating that the capsule has plugged the pore. Successive capsule profiles are shown on figure 13(*a*, *b*): the membrane gets very near the wall.

(ii) Exit plugging

In some instances, it is found that the capsule tends to touch the wall in the final transit phase, i.e. when the centre of mass has passed the throat. This phenomenon is illustrated for two particles, with radii 1.4 and 1.8.

Figure 14 shows the flow rate evolution with x_G for a capsule with radius 1.4 for three values of ϵ. As indicated previously, for $\epsilon = 0.03$, entry plugging is observed. For

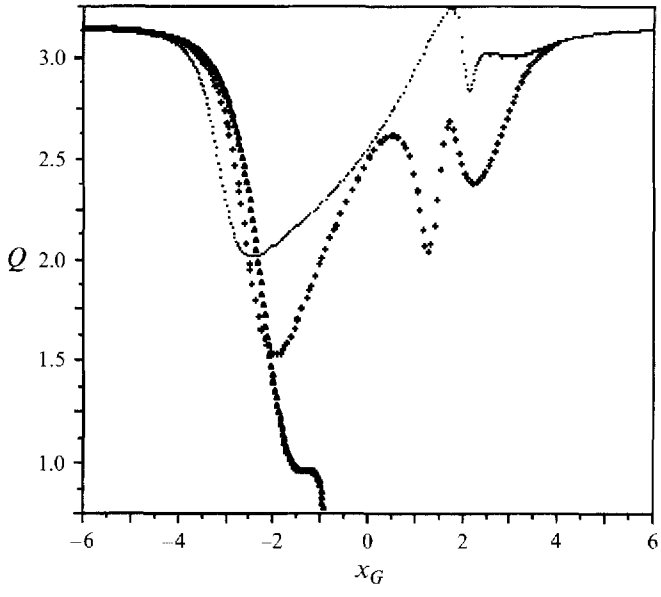

FIGURE 14. Effect of capillary number on flow rate Q ($R = 1.4$). ●, $\epsilon = 0.3$; +, $\epsilon = 0.1$; ▲, $\epsilon = 0.03$.

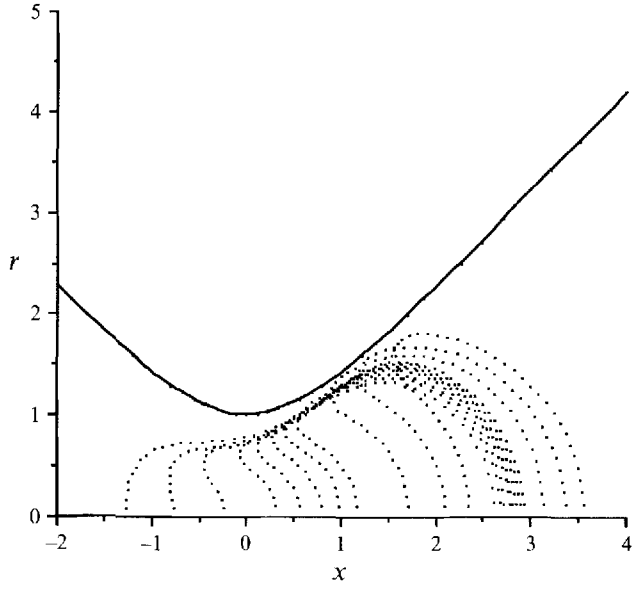

FIGURE 15. Successive profiles of a capsule ($R = 1.4$, $\epsilon = 0.1$). The membrane gets very near the wall, but the capsule eventually squeezes out.

$\epsilon = 0.3$, the capsule flows freely through the pore. For $\epsilon = 0.1$, the situation is not so clear. Indeed the flow rate ultimately goes back to its initial value, but after strong oscillations that correspond to successive compression/extension states of the membrane. In the recoil phase a parachute shape is observed for values of x_G quite close to the throat (figure 15). As the tail re-enters the capsule, the cusp produced tends to get very close to the wall, thereby slowing down the capsule and inducing a decrease in the flow rate (figure 14). In the region of cusps, where the lubrication film becomes

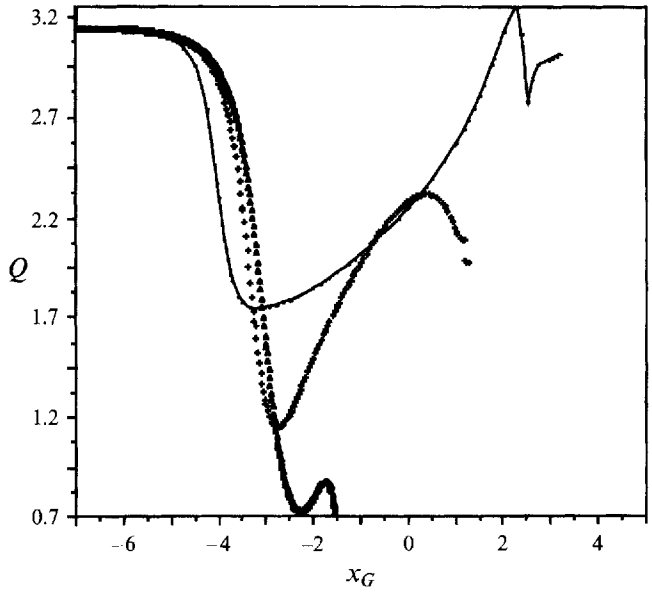

FIGURE 16. Effect of capillary number on flow rate Q ($R = 1.8$). —●—, $\epsilon = 0.3$; +, $\epsilon = 0.1$; ▲, $\epsilon = 0.05$.

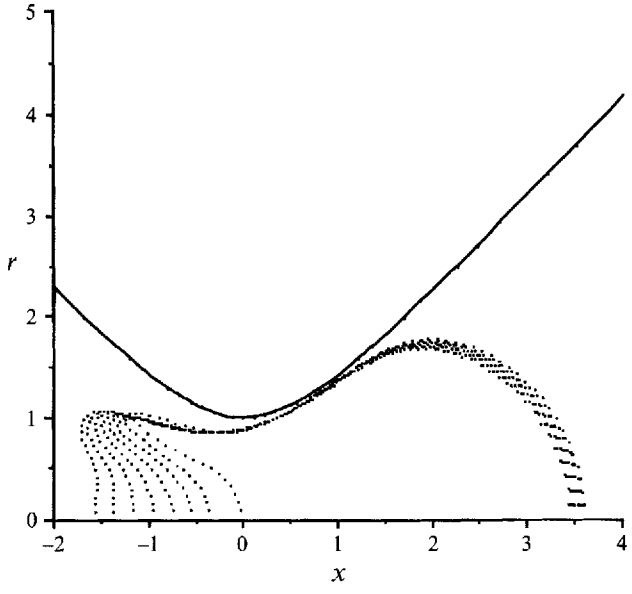

FIGURE 17. Successive profiles of a capsule ($R = 1.8$, $\epsilon = 0.1$). The capsule appears to be blocked during the exit process.

very thin, large oscillations of the force exerted by the wall on the fluid occur. The numerical precision then quickly deteriorates, but it was sometimes found useful to decrease the time step until the solution converged. In the case $R = 1.4$ and $\epsilon = 0.1$, the capsule gets dangerously near the wall, but manages ultimately to squeeze through.

Figure 16 represents the evolution of the flow rate for a larger capsule of initial radius 1.8 for $\epsilon = 0.05$, 0.1 and 0.3. The tendencies are similar to those just discussed. However, for $\epsilon = 0.1$ the flow rate evolution curve seems to indicate that the capsule

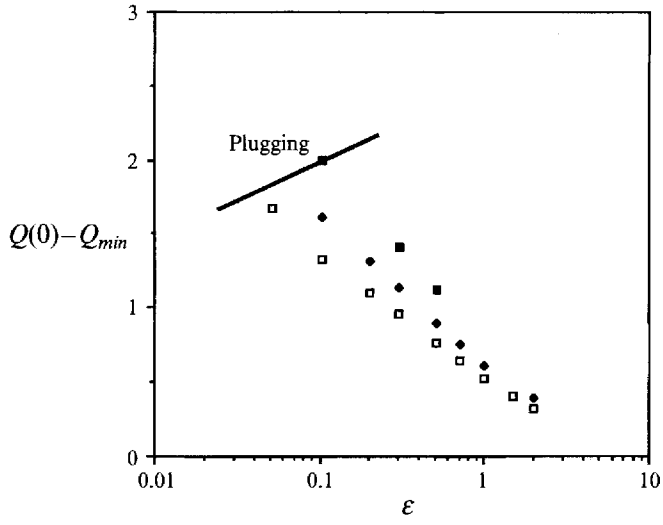

FIGURE 18. Maximum flow rate perturbation as a function of ϵ for capsules of initial radius: □, $R = 1.2$; ◆, $R = 1.4$; ■, $R = 1.8$. The plugging zone is indicated.

is blocked during the exit process. Figure 17 shows the successive last profiles observed before the capsule gets too near the wall and the process is stopped. However, the limit of validity of the model is definitely reached in this case. Indeed, along with the problems due to contact, cusps on the tail of the capsule are very sharp. The variations of the curvature in this area are large and difficult to compute with precision. Owing to these numerical limitations, it is not clear whether the capsule of figure 17 will be able to exit the pore or not.

A point in support of the occurrence of exit plugging is that clusters of blood cells stuck on the downstream side of filters are sometimes observed. These cells have reached the downstream side of the flow, but are stuck both to the membrane and to one another (Chien *et al.* 1984). This phenomenon is due to intermolecular interactions between the cells and the filter, and occurs when the distance between the cells and the filter wall becomes very small. Our model does not account for such physicochemical effects.

4.4. *Bulk variables of the flow*

A convenient way of representing the model predictions is to plot maximum flow rate perturbations as a function of ϵ and R (figure 18). This allows a comparison of the theoretical bulk results to the experimental data since changes in flow rate are commonly measured experimentally. The regressions that can be derived from these curves may then be used to interpret the filtration experiments of Drochon *et al.* (1993). The zone where plugging is expected or observed is also indicated on figure 18. However, the position of the frontier cannot be taken in a very precise sense. For large values of ϵ, the flow rate perturbation is quite small and fairly insensitive to capsule size. Cases where the longitudinal extension ratio becomes larger than 4 are dismissed, since most elastomer membranes would break in normal conditions.

Another parameter of interest is the so-called entry time t_e in the pore. It can be determined experimentally by means of an electrical method where the change of conductivity of a filter when one cell flows through is measured (Fischer, Wenby & Meiselman 1992). To be consistent with the experiment, t_e is defined here as the interval between the times where Q is decreased by 2% (i.e. $Q = 3.1$) and where Q is minimum.

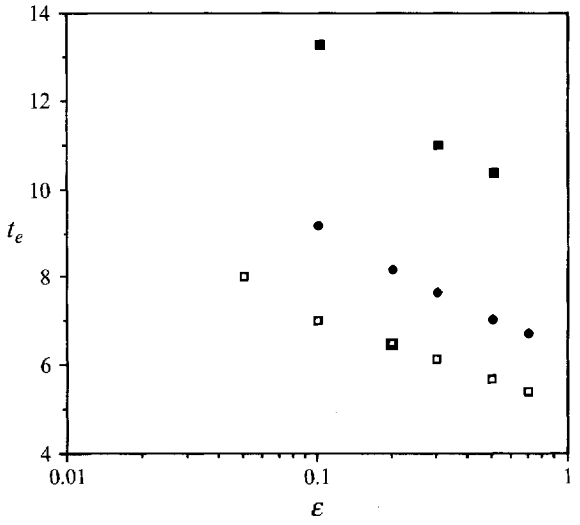

FIGURE 19. Entry time t_e in a pore as a function of ϵ for capsules of initial radius: □, $R = 1.2$; ◆, $R = 1.4$; ■, $R = 1.8$. The entry time is more sensitive to size ratio changes than to capillary number.

The evolution of t_e with ϵ and with R is shown on figure 19. As expected, the model predicts that the entry time increases with capsule size and rigidity. It is interesting that both figures 18 and 19 indicate that the capillary number has a smaller relative influence on Q or on t_e than the size ratio R. This means that filtration is not as sensitive to changes in membrane rigidity as to changes in capsule size.

5. Constant-flow-rate condition

Some experimental devices operate under constant-flow-rate conditions. The effect of the capsule may be measured in terms of additional pressure drop. However, to establish a direct comparison between constant-pressure-drop and constant-flow-rate systems, it is appropriate to introduce the apparent hydraulic resistance R_{Ha} of the pore:

$$R_{Ha}(t) = \frac{\Delta P(t)}{Q(t)}, \tag{5.1}$$

where $\Delta P(t)$ and $Q(t)$ are defined by (2.1) and (2.2), according to the flow conditions. The bulk effect of the flow-rate conditions is presented on figure 20 which shows the evolution of the relative perturbation of the hydraulic resistance as a function of x_G for $R = 1.4$ and $\epsilon = 0.1$, for constant pressure drop and constant flow rate. The curves are superimposed up to $x_G = -2.75$, showing that the evolutions of the capsule are similar up to this point. Then, $\Delta R_{Ha}/R_H$ becomes larger (maximum at 105%) for $\Delta P =$ constant than for $Q =$ constant (maximum at 70%). Finally, after some oscillations, the perturbation of the hydraulic resistance vanishes when the capsule has passed the throat, thus indicating that the particle has squeezed through in both cases. The evolution of the capsule shape in the recoil phase is shown in figure 21 for constant flow rate, and should be compared to figure 15. It appears, as expected, that the lubrication film in the most critical region is thicker for $Q =$ constant. Correspondingly $\Delta R_{Ha}/R_H$ is lower at $Q =$ constant. These results suggest that constant-pressure-drop systems may be more efficient (given the accentuated response) in discriminating between normally deformable and stiffened capsule membranes.

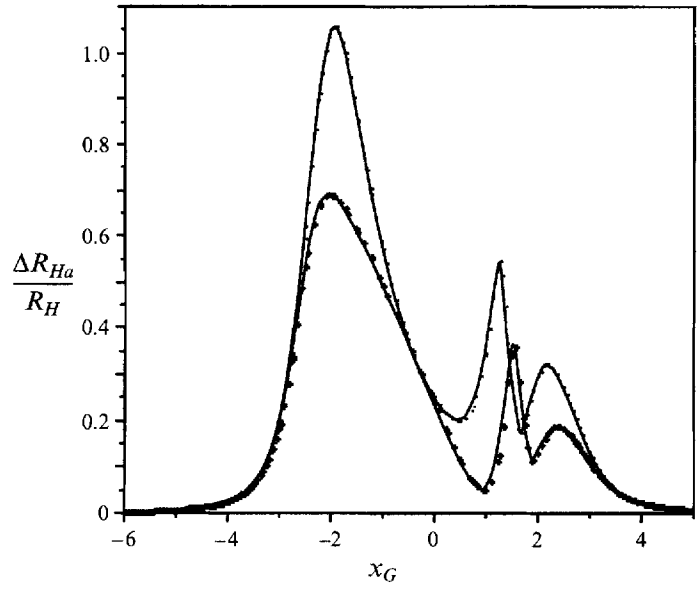

FIGURE 20. Evolution of the relative perturbation of the constriction hydraulic resistance as a function of x_G for $R = 1.4$ and $\epsilon = 0.1$: ●, constant pressure drop; +, constant flow rate.

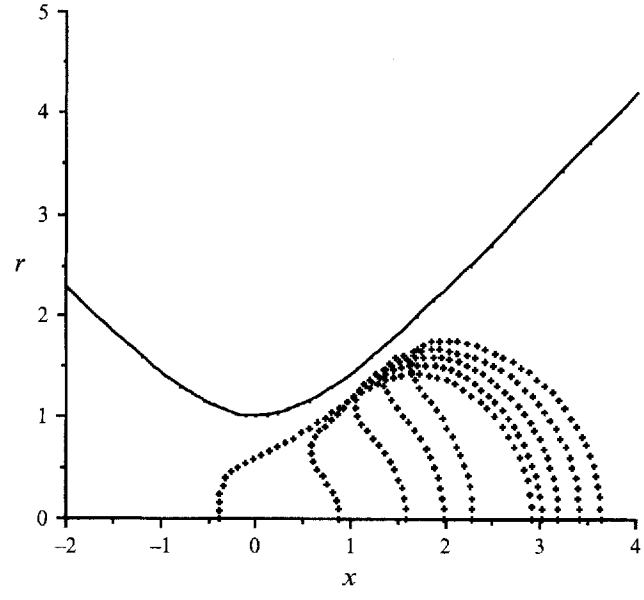

FIGURE 21. Successive profiles of a capsule ($R = 1.4$, $\epsilon = 0.1$) during the recoil phase, under constant-flow-rate conditions.

It is obviously of interest to compare a capsule that plugs the pore under a constant pressure drop to the same particle under constant-flow-rate conditions. Figure 22 shows the evolution of $\Delta R_{Ha}/R_H$ as a function of x_G for a capsule $R = 1.4$, $\epsilon = 0.03$ under the two types of flow conditions. The evolutions of $\Delta R_{Ha}/R_H$ are similar up to $x_G = -2.25$. At this point, owing to the dramatic decrease in flow rate the hydraulic resistance for the constant-pressure-drop flow goes to infinity as the capsule gets

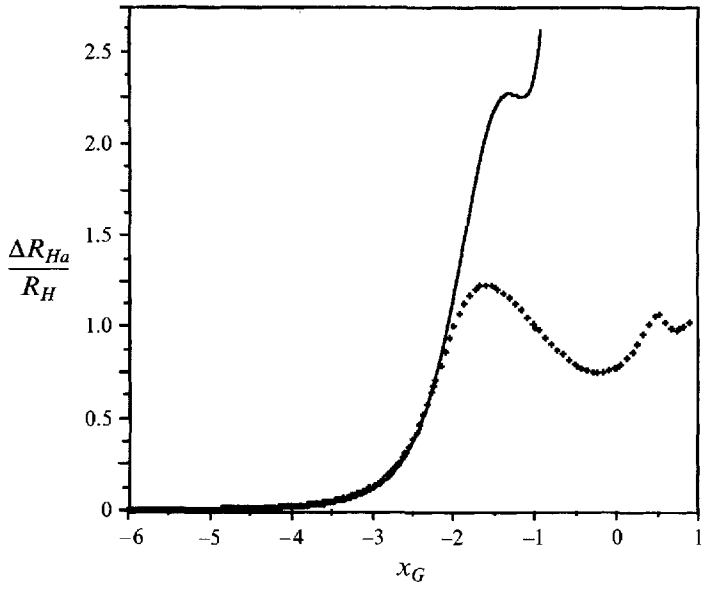

FIGURE 22. Evolution of the relative perturbation of the constriction hydraulic resistance as a function of x_G. Plugging occurs. $R = 1.4$ and $\epsilon = 0.03$. −, Constant pressure drop; +, constant flow rate.

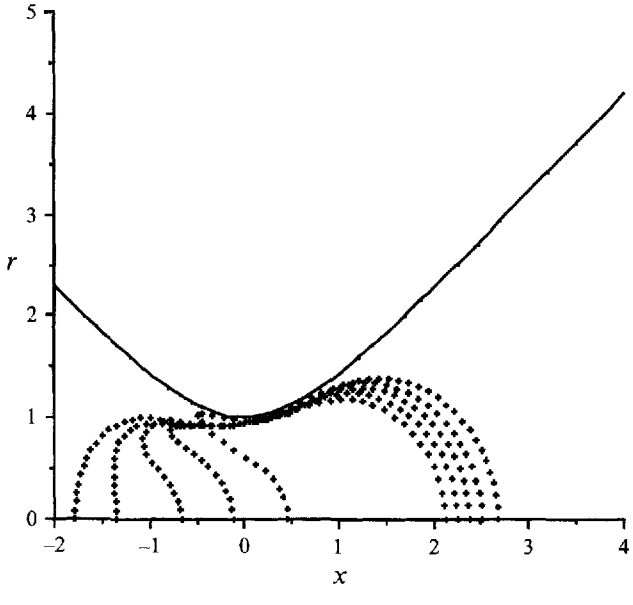

FIGURE 23. Successive profiles of a capsule ($R = 1.4$, $\epsilon = 0.03$) under a constant flow rate. Exit plugging seems to occur.

blocked at the entry of the pore. In the constant-flow-rate situation however, $\Delta R_{Ha}/R_H$ starts decreasing when $x_G > -1.75$ but the capsule tends to be stuck at the exit, as shown in figure 23, where the same kind of plugging pattern as in the case $R = 1.8$, $\epsilon = 0.1$ (figure 17) is observed.

Bulk results may be expressed in terms of the maximum perturbation of the apparent hydraulic resistance of the pore as a function of ϵ for a given size ratio ($R = 1.4$, figure

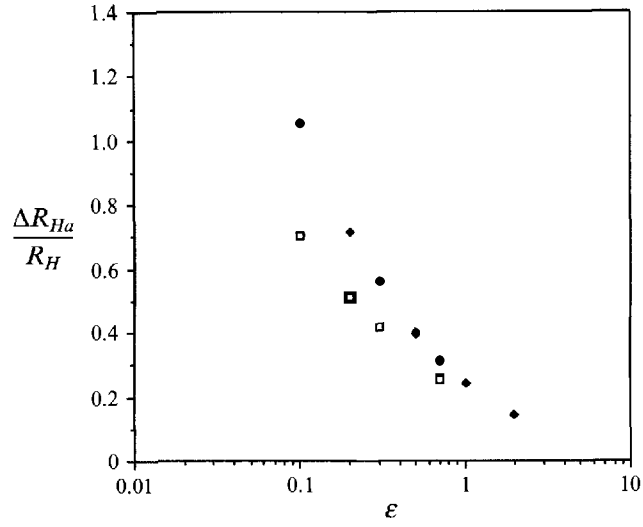

FIGURE 24. Evolution of the maximum relative perturbation of the hydraulic resistance as a function of ϵ (case $R = 1.4$). ◆, Constant pressure drop; □, constant flow rate.

24). As pointed out earlier, constant-flow-rate conditions produce a lower perturbation than constant-pressure-drop conditions but the difference tends to fade away for larger values of $\epsilon(\approx 1)$, where the level of perturbation is small in both cases.

6. Conclusion

The overall aim of the studies reported here has been to acquire fundamental knowledge on the microrheology and micromechanics of capsules and to provide theoretical data for the quantitative interpretation of filtration experiments. A comparison of the regressions obtained for the relative maximum decrease in flow rate as a function of ϵ at constant pressure head with the experimental decrease in flow rate reported by Drochon *et al.* (1993) for red blood cells the membrane of which has been artificially rigidified, shows that the model is able to predict only relative variations of E_s (Leyrat-Maurin, Drochon & Barthes-Biesel 1993). However, to interpret red-blood-cell filtration experiments in terms of the shear surface elastic modulus E_s of the cell, it is necessary to modify the membrane constitutive law. The red-blood-cell membrane is a lipid bilayer lined by a protein network. As such, it possesses shear elasticity (as measured by a modulus like E_s) and is also area incompressible. Constitutive laws that account for both properties have been proposed by Skalak *et al.* (1973) and by Evans (1973). Such a model is presently being developed and will be reported in a future communication.

This work was supported by CNRS and by Conseil Régional de Picardie, Pôle Modélisation.

REFERENCES

BARTHES-BIESEL, D. & RALLISON, J. 1981 The time-dependent deformation of a capsule freely suspended in a linear shear flow. *J. Fluid Mech.* **113**, 251–267.

BARTHES-BIESEL, D. & SGAIER, H. 1985 Role of membrane viscosity in the orientation and deformation of a spherical capsule suspended in shear flow. *J. Fluid Mech.* **160**, 119–135.

CHANG, K. S. & OLBRICHT, W. L. 1993 Experimental studies of the deformation and breakup of a synthetic capsule in steady and unsteady simple shear flow. *J. Fluid Mech.* **250**, 609–633.

CHIEN, S., SCHMID-SCHÖNBEIN, G. W., SUNG, K. L. P., SCHMALZER, E. A. & SKALAK, R. 1984 *Viscoelastic Properties of Leukocytes in White Cell Mechanics: Basic Science and Clinical Aspects*, pp. 19–51. Alan R. Liss, Inc.

DELVES, L. M. & MOHAMED, J. L. 1985 *Computational Methods for Integral Equations*. Cambridge University Press.

DROCHON, A. 1991 Détermination des propriétés mécaniques intrinsèques des hématies par viscosimétrie et filtration. PhD thesis, Université de Technologie de Compiègne.

DROCHON, A., BARTHES-BIESEL, D., BUCHERER, C., LACOMBE, C. & LELIEVRE, J. C. 1993 Viscous filtration of red blood cell suspensions. *Biorheology* **30**, 1–8.

DROCHON, A., BARTHES-BIESEL, D., LACOMBE, C. & LELIEVRE, J. C. 1990 Determination of the Red Blood Cell apparent membrane elastic modulus from viscometric measurements. *J. Biomech. Engng* **112**, 241–249.

EVANS, E. A. 1973 A new material concept for the red cell membrane. *Biophys. J.* **13**, 926–940.

FISCHER, T. C., WENBY, R. B. & MEISELMAN, H. J. 1992 Pulse shape analysis of RBC micropore flow via new software for the cell transit analyser (CTA). *Biorheology* **29**, 185–201.

GREEN, A. E. & ADKINS, J. C. 1960 *Large Elastic Deformation and Non-linear Continuum Mechanics*. Oxford University Press.

HAPPEL, J. & BRENNER, H. 1965 *Low Reynolds Number Hydrodynamics*. Prentice-Hall.

HELMY, A. & BARTHES-BIESEL, D. 1982 Migration of a spherical capsule freely suspended in an unbounded parabolic flow. *J. Méc. Théor. Appl.* **1**, 859–880.

KELLER, S. R. & SKALAK, R. 1982 Motion of a tank-treading ellipsoidal particle in a shear flow. *J. Fluid Mech.* **120**, 27–47.

LADYZHENSKAYA, O. A. 1969 *The Mathematical Theory of Viscous Incompressible Flow*. Gordon and Breach.

LEYRAT-MAURIN, A., DROCHON, A. & BARTHES-BIESEL, D. 1993 Flow of a capsule through a constriction: application to cell filtration. *J. Phys. Paris* III, **3**, 1051–1056.

LI, X. Z., BARTHES-BIESEL, D. & HELMY, A. 1988 Large deformations and burst of a capsule freely suspended in an elongational flow. *J. Fluid Mech.* **187**, 179–196.

LONGUET-HIGGINS, M. S. & COKELET, E. D. 1976 The deformation of steep surface waves on water. I. A numerical method of computation. *Proc. R. Soc. Lond.* A **350**, 1–26.

MARTINEZ, M. J. & UDELL, K. S. 1990 Axisymmetric creeping motion of drops through circular tubes. *J. Fluid Mech.* **210**, 565–591.

POZRIKIDIS, C. 1990 The axisymmetric deformation of a red blood cell in uniaxial straining Stokes flow. *J. Fluid Mech.* **216**, 231–254.

POZRIKIDIS, C. 1992 *Boundary Integral and Singularity Methods for Linearized Viscous Flow*. Cambridge University Press.

RALLISON, J. M. & ACRIVOS, A. 1978 A numerical study of the deformation and burst of a viscous drop in an extensional flow. *J. Fluid Mech.* **89**, 191–200.

SECOMB, T. W., SKALAK, R., OZKAYA, N. & GROSS, J. F. 1986 Flow of axisymmetric red blood cells in narrow capillaries. *J. Fluid Mech.* **163**, 405–423.

SKALAK, R., TOZEREN, A., ZARDA, R. P. & CHIEN, S. 1973 Strain energy function of red blood cell membranes. *Biophys. J.* **13**, 245–264.

SUTERA, S. P., PIERRE, P. R. & ZAHALAK, G. I. 1989 Deduction of intrinsic mechanical properties of the erythrocyte membrane from observations of tank-treading in the rheoscope. *Biorheology* **26**, 177–197.

TÖZEREN, H. & SKALAK, R. 1979 The flow of closely fitting particles in tapered tubes. *Intl J. Multiphase Flow* **5**, 395–412.

TRAN-SON-TAY, R., SUTERA, S. P. & RAO, P. R. 1984 Determination of red blood cell membrane viscosity from rheoscopic observations of tank-treading motion. *Biophys. J.* **46**, 65–72.

YOUNGREN, G. K. & ACRIVOS, A. 1975 Stokes flow past a particle of arbitrary shape: a numerical method of solution. *J. Fluid Mech.* **69**, 377–403.

YOUNGREN, G. K. & ACRIVOS, A. 1976 On the shape of a gas bubble in a viscous extensional flow. *J. Fluid Mech.* **76**, 433–442.